Title: **Occurrence rates of SuperDARN ground scatter echoes and electron density in the ionosphere**

Alexander V. Koustov
Department of Physics and Engineering Physics, University of Saskatchewan, Saskatoon, Saskatchewan, Canada
e-mail: sasha.koustov@usask.ca

Sydney Ullrich
Department of Physics and Engineering Physics, University of Saskatchewan, Saskatoon, Saskatchewan, Canada
e-mail: sju861@mail.usask.ca

Pavlo V. Ponomarenko
Department of Physics and Engineering Physics, University of Saskatchewan, Saskatoon, Saskatchewan, Canada
e-mail: pasha.ponomarenko@usask.ca

Mehdi Ghalamkarian Nejad
Department of Physics and Engineering Physics, University of Saskatchewan, Saskatoon, Saskatchewan, Canada
e-mail: meg698@mail.usask.ca

David R. Themens
Department of Physics, University of New Brunswick, Fredericton, NB, Canada and Space Environment and Radio Engineering Group, School of Engineering, University of Birmingham, Birmingham, UK
e-mail: david.themens@gmail.com

Robert G. Gillies
Department of Physics and Astronomy, University of Calgary, Calgary, Alberta, Canada
e-mail: rgillies@ucalgary.ca

Correspondence to: A.V. Koustov, sasha.koustov@usask.ca

Key points

▪ Occurrence rate of SuperDARN grounds scatter increases with peak electron density increase. The trend saturates at large electron densities

▪ Midlatitude SuperDARN radars show dayside maxima in occurrence of ground scatter in winter, consistent with winter anomaly phenomenon

▪ Polar cap SuperDARN radars show summer maxima in occurrence of ground scatter both at daytime and nighttime

Keywords: midlatitude winter anomaly, electron density, SuperDARN radars, ground scatter occurrence rate, incoherent scatter radars RISR, CADI ionosonde

Abstract

Ground scatter (GS) echoes in Super Dual Auroral Radar Network (SuperDARN) observations have been always expected to occur under high-enough electron density in the ionosphere providing sufficient bending of HF radio wave paths toward the ground. In this study we provide direct evidence statistically supporting this notion by comparing the GS occurrence rate for the Rankin Inlet SuperDARN radar and the F region peak electron density N_mF_2 measured at Resolute Bay by the CADI ionosonde and incoherent scatter radars RISR-N/C. We show that the occurrence rate increases with N_mF_2 roughly linearly up to about $\sim 4\cdot10^{11}\ \mathrm{m}^{-3}$ and the trend saturates at larger N_mF_2. One expected consequence of this relationship is correlation in seasonal and solar cycle variations of the GS echo occurrence rate and N_mF_2. GS occurrence rates for a number of SuperDARN radars at middle latitudes, in the auroral zone and in the polar cap are considered separately for daytime and nighttime. The data indicate that the daytime occurrence rates are maximized in winter and nighttime occurrence rates are maximized in summer for middle latitude and auroral zone radars in the Northern Hemisphere, consistent with the Winter Anomaly (WA) phenomenon. The effect is most evident in the North American and Japanize sectors, and the quality of WA signatures deteriorates in the European and, especially, in the Australian sectors. The effect does not exist in the South American sector and in the polar caps of both hemispheres.

Introduction

High-frequency (HF) radio waves transmitted into the Earth's ionosphere can experience significant refraction or even be reflected from ionospheric layers of enhanced ionization so that they turn to the ground and reach it some distance away from a transmitter. The wave energy then can be either forwarded farther back into space or returned to the transmitter via scattering from roughness of the Earth's surface. Such returned signals are often called ground scatter (GS), e.g. Davis (1969). GS is a ubiquitous feature of Super Dual Auroral Radar Network (SuperDARN) HF radar records (Chisham et al., 2007; Nishitani et al., 2019).

Ground scatter echoes detected by SuperDARN have been extensively used for studies of various ionospheric phenomena, for example for assessing gravity waves' parameters and locating their sources (Karhunen et al., 2006; Samson et al., 1990), for investigation of the medium-scale travelling ionospheric disturbances at middle latitudes (Grocott et al., 2013; Frissell et al., 2014; 2016; Oinats et al., 2016), the nature of geomagnetic pulsations (Ponomarenko et al., 2003; 2005) and regional anomalies in the electron density distribution in the ionosphere (de Larquier et al., 2011; Milan et al., 2013). GS echoes are also useful for estimates of the electron density in the ionosphere (André et al., 1998; Bland et al., 2014).

Despite decades of SuperDARN research and numerous publications involving ground scatter (e.g., reviews by Chisham et al., 2007 and Nishitani et al., 2019) and generally well-accepted mechanism of such signals' formation, several aspects of these echo observations are still not well investigated and understood. Quantitative information on the occurrence of GS echoes at various latitudes has not been widely discussed, contrary to the case of ionospheric echoes (e.g., Ghezelbash, 2013; Ghezelbash et al., 2014a,b). This is, perhaps, because the primary goal of the SuperDARN radar experiment is plasma flow monitoring, and GS is literally a nuisance in achieving this goal. One interesting and important topic in SuperDARN GS research is occurrence rate of these echoes and factors affecting their onset. Of interest are the solar cycle, seasonal and diurnal variations of GS echo occurrence (e.g., Marcucci et al., 2021).

It has also been recognized that additional HF radio wave absorption in the *D* region is another key factor to be taken into consideration (Chakraborty et al., 2018; Fiori et al., 2018; Watanabe & Nishitani, 2013). An important role of the Earth's surface roughness in returning radio waves back to a radar has been emphasized (Barrell et al., 2016; Ponomarenko et al., 2009; Shand et al., 1998) but quantitative assessment of the effect is not an easy task. In terms of factors affecting GS echo occurrence rate, it has always been accepted that radio waves turning towards the ground is a key process for detection of GS. However, the ionospheric electron density "threshold" required for steady detection of SuperDARN GS echoes has never been discussed. All-in-all, the threshold conditions in the ionosphere for detection of SuperDARN GS echoes require investigation.

The present paper has two major goals. One is to establish statistically whether GS occurrence rate increases with the electron density in the ionosphere. We target GS echo detection via the *F* region and possible correlation with the peak electron density N_mF_2. Our second goal is to investigate long-term trends in the occurrence of SuperDARN GS echoes, such as solar cycle and seasonal variations, and to establish whether these trends are consistent with changes of N_mF_2. We focus on differences between daytime and nighttime GS echo occurrence rates as these observations are affected by the roughness and conductivity of the Earth's surface similarly. We group SuperDARN radars according to their field-of-view (FOV) location, at middle latitudes, auroral zone latitudes and at extreme high latitudes, in the polar cap.

2. Modeling of ground scatter signals

For better understanding of the issues addressed in this study, we give a brief description of HF GS radar signal formation.

HF radio waves transmitted into the ionosphere experience refraction controlled by the electron density distribution in the ionosphere. To evaluate possible paths of waves, a 3-D analysis is generally required, but many major features of HF radio wave propagation in the ionosphere can be illustrated by considering a 2-D model of the electron density distribution with changes only vertically and with the distance from a radar. In a case of smooth spatial variations, such as those given by statistical ionospheric models (e.g., the E-CHAIM model, Themens et al. (2017, 2019)), the application of Snell's law is straightforward for ray tracing. The tracings presented below have been done with one additional effect. The ionosphere contains inhomogeneities of various scales. They affect radio wave paths locally and can potentially introduce significant deviations of radio wave paths from those expected for a "smooth" ionosphere (e.g., Uspensky et al., 1993). Such effects are typically ignored in HF propagation analysis because detailed information on localized inhomogeneities is seldom available. In our ray tracings, we included their effects by introducing a random local tilt of an ionospheric layer at a refraction point of a layer, at every step of calculations, and allowing random departures of the tilt from the large-scale density trend given by the E-CHAIM model. The random tilts were assigned according to Gaussian distribution with zero mean and width of $1°$.

Figure 1 shows possible radio wave paths in the ionosphere for the Rankin Inlet (RKN) SuperDARN radar along its beam 7 for the transmitter frequency of 12 MHz. Two extreme cases are considered, with low electron density (Figure 1a, 00 UT, local dusk) and high electron density (Figure 1b, 18 UT, local noon). The electron density distributions (2-D) were adopted according to the E-CHAIM electron density model (Themens et al., 2017, 2019) for 10 March 2016. The E-CHAIM based electron density were multiplied by a factor of 1.25 at every height to achieve qualitative overall agreement between the modeled and observed bands of GS and ionospheric echo bands. In Figure 1, white and red markers correspond to group range gates 0, 10, 20… and 5, 15, 25 …, respectively. We remind the reader that the slant range to an echoing region in SuperDARN observations is computed as $range(km) = 180 + 45 \times (range\ gate)$. Yellow markers at ionospheric heights in Figure 1 are locations from where ionospheric echoes can be detected if decameter irregularities are present. Magenta markers on the ground are those locations from where a ground scatter signal can be received.

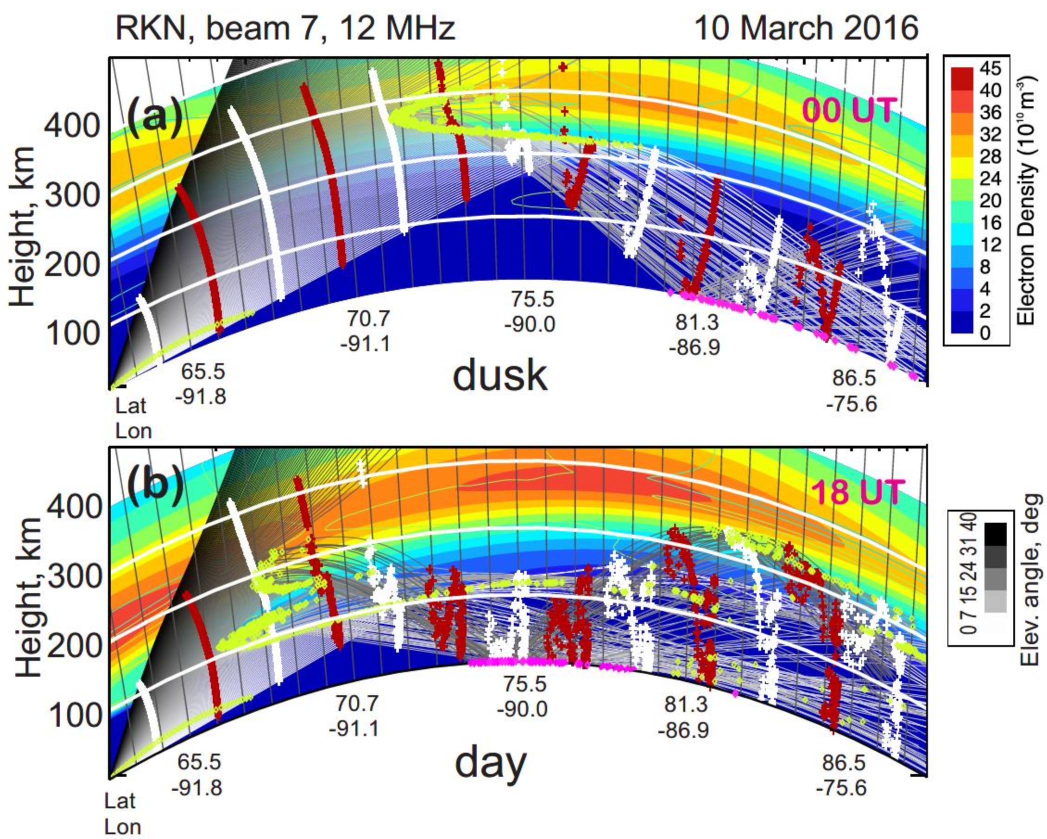

Figure 1: Ray tracing for 12 MHz radio waves transmitted by the Rankin Inlet (RKN) radar along its beam 7. The 2-D electron density distribution, represented by the color contours, is according to the E-CHAIM electron density model (Themens et al., 2017, 2019) with all values for (a) 00 UT and (b) 18 UT on 10 March 2016 increased by 1.25. White and red markers correspond to group range gates 0, 10, 20 … and 5, 15, 25…, respectively. Yellow markers at ionospheric heights mark those locations from where the ionospheric echoes can be detected while magenta markers on the ground are those locations from where the ground scatter echoes can be detected.

Figure 1a for dusk conditions shows that while ionospheric echoes can come anywhere from range gates 25 and 40, the GS echoes are expected from range gates 45-60. Figure 1b for noon conditions shows that both ionospheric and GS echoes are generally coming from shorter ranges. Interestingly, GS echoes can be received via *E* region (~100 km heights), as well as via *F* region (~200 km). This is because the electron density is larger during daytime, an easily recognizable feature from the electron density color contours in Figures 1a and1b at heights around ~300 km. Distinguishing GS from the *E* and *F* regions in observations is difficult during these periods because the range gates can be close to each other.

To model the GS echo power distribution with range, we performed a number of tracings so that the total number of wave ground hits would be on the order of ~1000. The average power of echoes in each 45-km gate along the radar beam was then computed by assuming that the power is proportional to the number of rays reached this specific range gate and assuming that the radio wave power decays inversely proportional to the cube of the range. Contributions from high and low beams were summed together.

Figure 2 shows the range gate distribution of the expected GS echo power (expressed in dBs from an arbitrary level) at two radar frequencies of 10 and 12 MHz and for 4 periods, local dusk (00 UT), midnight (06 UT), dawn (12 UT) and noon (18 UT) for the event considered. All plots show that the echo power range profile has a maximum at shorter ranges within every band, and the echo power decays more slowly at farther ranges. For noon (18 UT), a second 12 MHz band at larger ranges is seen. All the plots also show that 10 MHz echo bands are shifted toward shorter ranges by ~ 5 range gates. Finally, the plots show that the bands as a whole are shifted toward smaller range gates at noon as compared to other time sectors. The last two features are expected because the electron density is largest on the dayside for the RKN field of view.

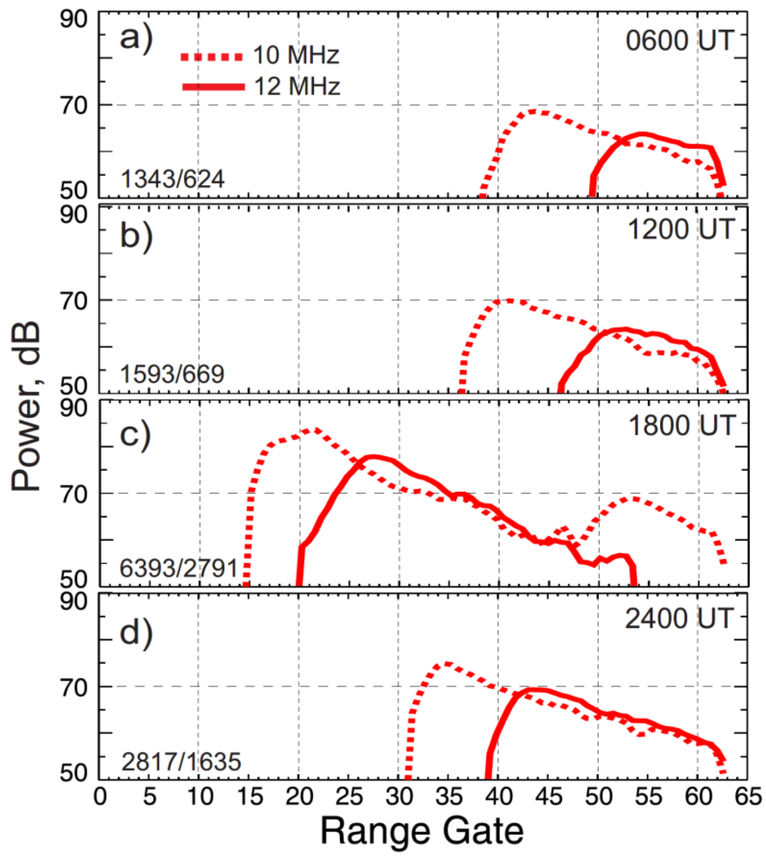

Figure 2: The expected power (in dB with respect to an arbitrary level) of ground-scattered echoes for various radar range gates of the SuperDARN Rankin Inlet (RKN) radar in beam 7 at operating frequencies of 10 and 12 MHz. Four panels correspond to observations the (a) midnight (06 UT), (b) dawn (12 UT), (c) daytime (18 UT) and (d) dusk (00 UT) sectors. A case of 10 March 2016 was considered (Figure 1 shows modeling for 00 UT and 18 UT). Details of the modelling approach are given in the text and in Koustov et al. (2020b). Numbers in the left-bottom corner of each panel indicate the total number of rays that formed the ground scatter range profiles at 10 and 12 MHz, respectively.

3. A comparison of the peak electron density in the ionosphere and occurrence of ground scatter

We explore now whether an increase in the peak electron density in the ionospheric *F* region N_mF_2 correlates with an increase in the occurrence rate of GS signals detected by the Rankin Inlet SuperDARN radar. The reason for the RKN radar selection is that, within its field of view, routine measurements of N_mF_2 are carried out at Resolute Bay (RB) with CADI ionosonde (Jayachandran et al., 2009) and occasional experiments are carried out with the Resolute Incoherent Scatter Radars, RISR-North and RISR-Canada (Gillies et al., 2019). The RB zenith corresponds to the RKN range gate 26 at the height of ~300 km. Another reason for this radar selection is that sporadic *E* layers, occasionally blocking HF radio waves' access to the *F* region (Cameron et al., 2022) are not a frequent phenomenon in the polar cap (McDougall et al., 2000), especially on the nightside.

Since RKN GS echoes are usually detected in a wide band of range gates, from 10 to 50-60, a better coverage with electron density measurements would be beneficial for the issue under investigation but none of the SuperDARN radars have such a desired coverage and only few have one or two ionosondes. Another important feature of the RKN radar is that its antennae has specially-installed wire mesh at the back of the antenna so that the radar mostly detects echoes from the antennae front side. This removes one of the uncertainties in SuperDARN GS measurements (Burrell et al., 2018). In this study, the GS was identified according to the standard method introduced by Blanchard et al. (2009).

For the comparison, first, RB CADI ionosonde observations from 2007 to 2019 were considered with critical frequencies f_0F_2 being scaled from ionograms collected typically with 15-min resolution, except for special experiments (for example, joint experiments with the RISR radars) for which up to 1-min ionograms were available.

A second and independent data set was created by considering RISR electron density profiles (2016-2019) for both the WorldDay mode (11-beam experiments) and the Imaging mode (51-beam experiments) measurements with 5-min resolution and with beams at elevation angles above 55° so that the data would correspond to the RB zenith. Individual electron density profiles from multiple beams were averaged and then fit with a polynomial of the 3-rd order near the profile maximum to identify the peak electron density.

The occurrence rate of RKN GS echoes in every 15-min interval of a day were computed for every range gate and beams 4-6 oriented toward RB (see maps in Koustov et al., 2020a,b, Figure 2). The rates were computed as the ratio of the number of detected echoes over the total number of transmissions in specific beams). The rates were matched with the N_mF_2 inferred from either CADI or RISR observations.

Two time sectors of the comparison were selected for presentation - nighttime (03-09 UT) and daytime (15-21 UT) reflecting extremes in terms of sunlight/ionospheric conditions. Figure 3 summarizes results of the comparison, separately for nighttime (left column) and daytime (right column). Color panels of Figures 3a and 3b show GS occurrence rate as a function of N_mF_2 (in steps of $0.25 \cdot 10^{11}\ \mathrm{m}^{-3}$). One visible effect on both panels is generally larger range gate numbers of bands with enhanced GS occurrence rate at night. Also noticeable is a progressively larger shift of the echo bands closer to the radar at larger N_mF_2. Both effects are expected, as discussed in the previous section (Figure 2).

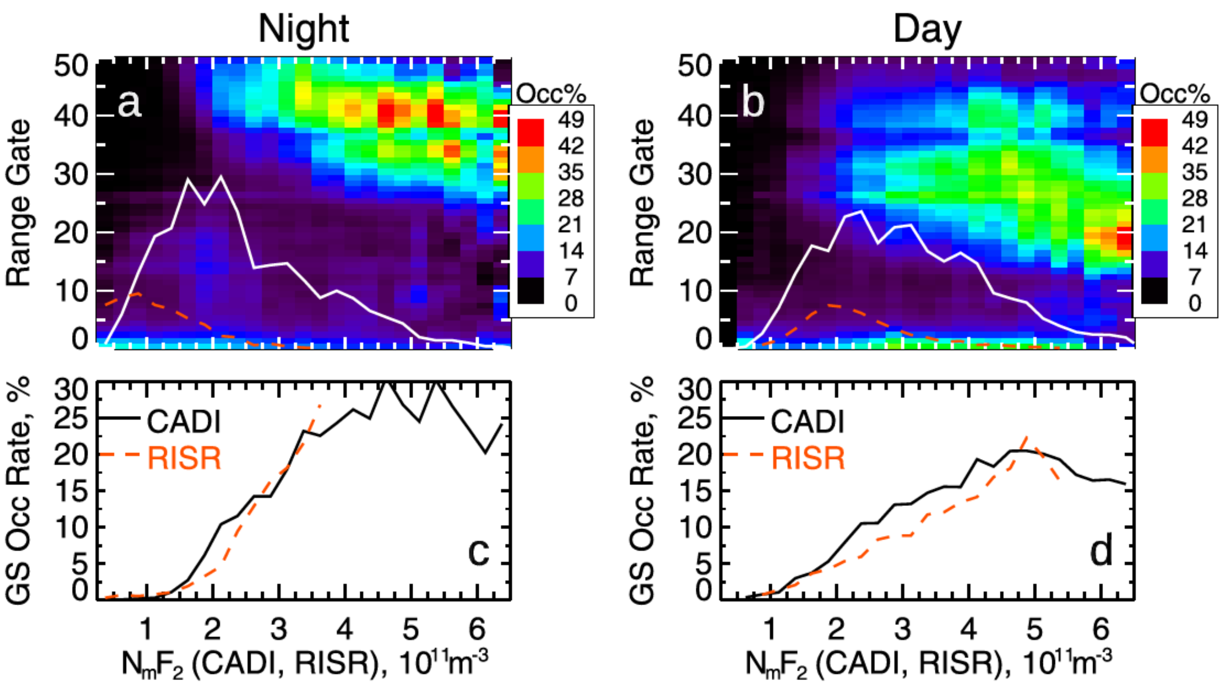

Figure 3: Ground scatter (GS) occurrence rate (over 15-min intervals) for the Rankin Inlet (RKN) SuperDARN radar observations in beams 4-6 at various range gates as a function of the *F* region peak electron density N_mF_2 measured concurrently by the Resolute Bay CADI ionosonde (a) for nighttime (03-09 UT) and (b) daytime (15-21 UT). Solid white lines indicate the number of available joint points (counts were divided by 40). (c) Line plot of the average GS occurrence rate over the band of ranges (gates 30-50 for nighttime and 20-40 for daytime), given as a solid line, versus N_mF_2 for joint observations with CADI at (c) nighttime and (d) daytime. N_mF_2 bins of $0.25 \times 10^{11}\ \mathrm{m}^{-3}$ were implemented. Dashed lines in all panels show the same dependence but for joint observations of the RKN and RISR radars.

To explore the correlation of GS occurrence rate upon N_mF_2 in a more quantitative manner, we show by solid lines the average occurrence rate over the band of range gates 30-50 on the nightside and 20-40 on the dayside, Figures 3c and 3d, respectively. The slightly different span of echo bands for nighttime and daytime were chosen because of the mentioned above general difference in the band locations.

The trend in GS occurrence rate increase is obvious in both plots of Figures 3c and 3d. Also "saturation" in the rate of increase at large N_mF_2 is evident. The saturation is visible at N_mF_2 >

$\sim 4\cdot 10^{11}\ \mathrm{m}^{-3}$. The level of saturation is higher at nighttime. Unfortunately, for both plots, the number of joint observations drops down dramatically at highest N_mF_2, see white lines reflecting the number of CADI-RKN measurements (the actual values were reduced by 40 times, and the scale on the left can be used to evaluate the actual numbers). The data coverage can be considered as reasonable for N_mF_2 up to $\sim 5\cdot 10^{11}\ \mathrm{m}^{-3}$ with the number of points in individual pixels reaching ~100.

Similar analysis and assessment have been done for joint RISR – RKN data set (color panels are not presented in Figure 3). The average occurrence rates over the bands of enhanced GS occurrence are presented in Figures 3c and 3d by red dashed lines. The number of points for this comparison is shown in Figures 3a and 3b by dashed red lines (the actual values were reduced by 40 times, and the scale on the left can be used to evaluate the actual numbers). These observations cover low end of values involved in the comparison with CADI. The occurrence rate- N_mF_2 curves for the RISR-RKN comparison are both similar to those obtained for the CADI-RKN comparison, see Figures 3c and 3d. Unfortunately, no RISR data above $\sim 4\cdot 10^{11}\ \mathrm{m}^{-3}$ are available so that whether “saturation” in the trend occurs is impossible to determine.

4. Typical ground scatter band location for the Saskatoon SuperDARN radar

Our goal now is to investigate whether long-term variations in the GS occurrence rate on the dayside and nightside are governed by the expected variations of N_mF_2.

Figure 4 presents GS occurrence rates at various range gates for the Saskatoon (SAS) SuperDARN radar at nighttime (left column) and daytime (right column) between range gates 0 and 50 and for the period of 2013-2018. Observations in beams 5-10 (looking poleward) and all radar frequencies were considered. For both time sectors in Figure 4, frequent occurrence of short-range GS echoes (gates 0-3) is evident. These echoes have been the subject of a targeted study by Ponomarenko et al. (2016) and they will not be discussed here. The primary interest in this study is GS echoes at range gates 20-50. These are well seen as “islands” centered on winter with more obvious and consistent pattern for the daytime. Strong decay in occurrence rate toward 2018 is seen. The effect is consistent with the decay in the solar activity as indicated by the F10.7-cm flux data, see for example Figure 4a in Koustov et al. (2019). Less obvious features in the patterns of enhanced GS occurrence in Fig 4 are 1) overall, larger detection rates at closer range gates for the periods of higher solar activity (well seen for the daytime data) and 2) shifts of echo bands with enhanced echo occurrence toward larger gates with the time off the winter (seen as more “curve”-shaped areas with enhanced echo occurrence). These and other details of these features for the HOK SuperDARN radar have been investigated by Oinats et al. (2016), and what we see in our plots are consistent with the modeling by Oinats et al. (2016).

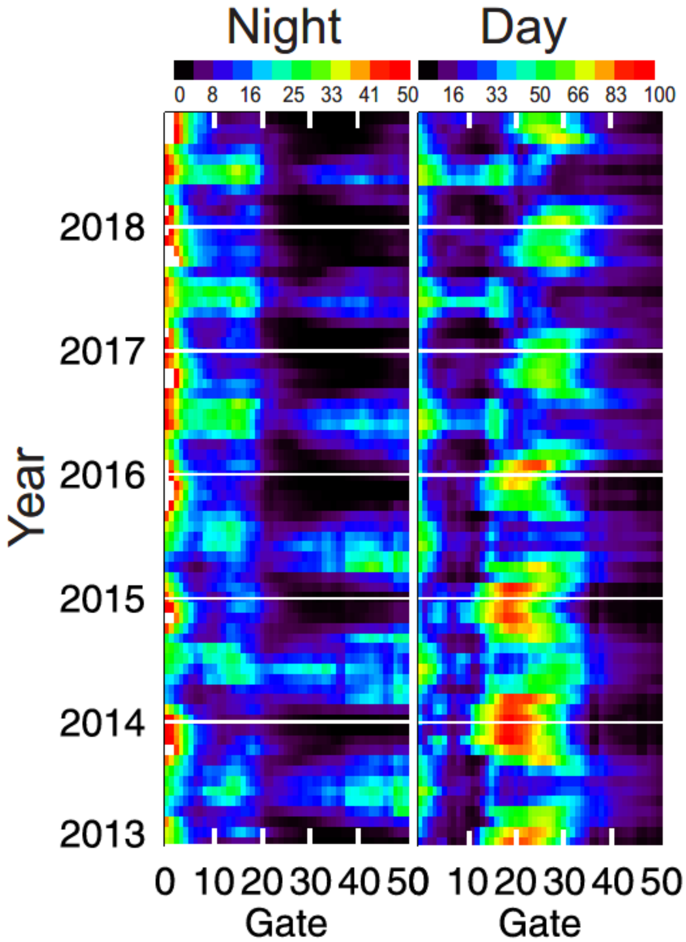

Figure 4: Occurrence rate of ground-scattered (GS) echo detection by the Saskatoon (SAS) SuperDARN radar at various ranges (range gates) in all beams irrespective of radar frequency for observations in 2013-2018. Left column are data for the nighttime (0300-0900 UT) while right column are data for daytime (1500-2100 UT). Notice that that the scale (color bars at the top) for the nighttime occurrence rate is half of that for the daytime occurrence rate.

Another noticeable feature in plots of Figure 4 is a separate region with enhanced echo occurrence rate at range gates 15-20, predominantly in summer. These are well recognizable at the nighttime plots. During daytime, such regions are well seen only during the years of low solar activity (2016-2018) and these regions "overlap/merge" with the regions of enhanced GS occurrence at higher range gates that shift to shorter ranges under high solar activity. The short-range regions of enhanced echo occurrence are likely related to the onset of relatively strong *E* region electron density at daytime or sporadic *E* layers at nighttime. Misidentification of nighttime echoes as GS is likely another reason for the nighttime cluster of short-range echoes as *E* region echoes are particularly in abundance at nighttime (Makarevich et al., 2002). The overlap of GS echoes received through the *F* region and *E* region is expected when the *E* region electron density is enhanced. Such cases are seen in Figure 1b during noon hours for the considered event.

One conclusion from plots of Figure 4 is that if one wants to capture variations in GS echo occurrence for the SAS radar in general, one can consider occurrence rates for gates 10-50, but keep in mind that some summer echoes also originate from ray bending at the *E* region heights.

5. Seasonal variations of GS echoes in Saskatoon and *F* region peak electron density

In this section, we investigate seasonal variations in average SAS GS occurrence rate and its correlation with electron density N_mF_2 variations. The SAS radar detects echoes from regions close to the equatorial/central part of the auroral oval. We computed the average GS echo occurrence for all beams and gates 10-50 with 15-min resolution in four sectors: night (03-09 UT), dawn (09-15 UT), day (15-21 UT) and dusk (21-24 UT) but only data for daytime and nighttime are presented here, Figure 5. Figure 5 shows the data trends obtained by applying smoothing with +/- 15-day boxcar filter. Figure 5 also shows electron density N_mF_2 variations for nighttime and daytime as given by the E-CHAIM ionospheric model (Themens et al., 2017, 2019) for each 15-min interval of SAS occurrence computations and smoothed with the same filter.

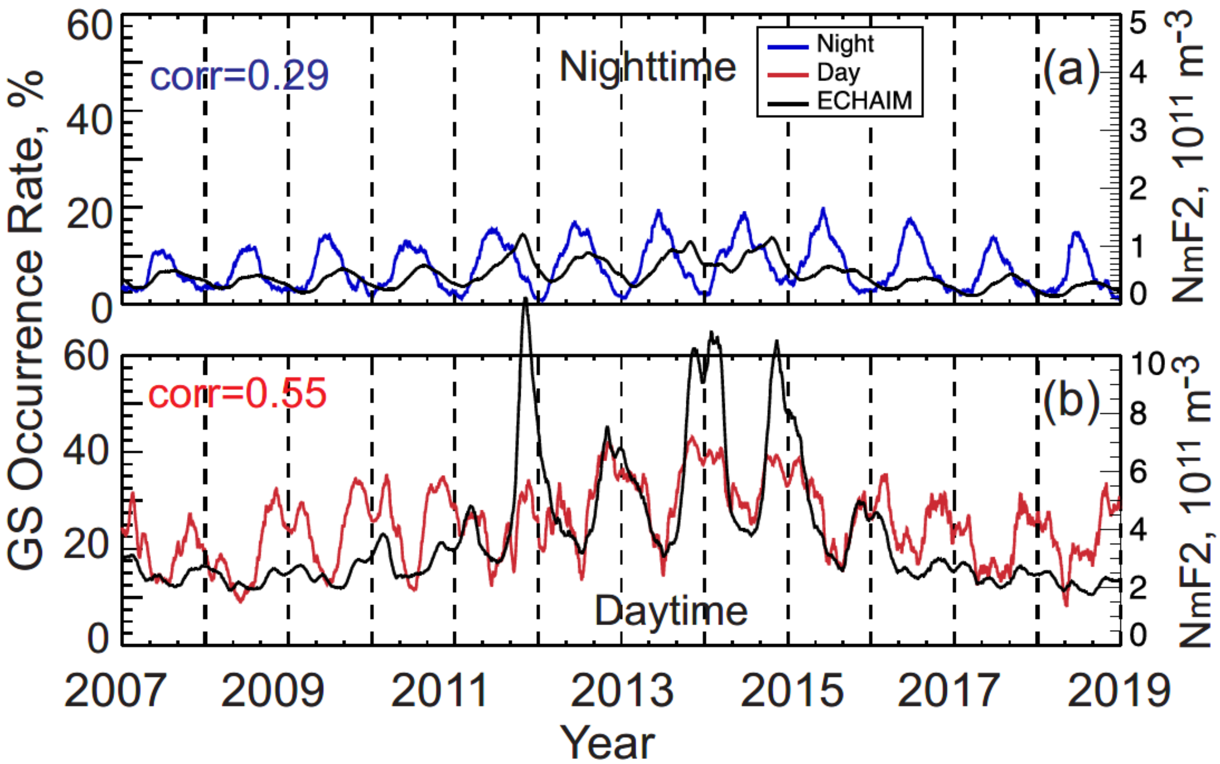

Figure 5: Line plots of the ground scatter (GS) occurrence rate for the Saskatoon SuperDARN radar in all beams averaged over range gates 10-50 for (a) nighttime (0300 and 0900 UT) and (b) daytime (1500-2100 UT) observations between 2007 and 2019. Transmissions on all radar frequencies were considered. The 15-min occurrence values were smoothed by applying a running +/- 15 day boxcar filter. Black line is the electron density N_mF_2 according to the E-CHAIM ionospheric model (Themens et al., 2017, 2019) computed for 15-min intervals and smoothed by applying a running +/- 15 day boxcar filter. In each panel, Pearson correlation coefficient (corr) between variations of the GS occurrence rate and N_mF_2 is presented.

Figure 5a indicates that the nighttime GS occurrence rate consistently reaches maxima in the summer and minima in the winter. The values of nighttime maxima are larger at high solar activity (2012-2015) so that crest-to-peak ratios of variations are somewhat larger during high solar activity period (2012-2015). Figure 5a also shows that the electron density N_mF_2 maximizes around summer, but not for every year considered. For some years, the N_mF_2 maxima are shifted to the fall equinoctial time (2011-2014). The effect is known for midlatitude observations (Richardson, 2001). Even though the N_mF_2 and GS occurrence rate curves have clear single peaks, the correlation between variations of N_mF_2 and GS occurrence rate is rather weak, the Pearson correlation coefficient is only 0.29.

Seasonal variations of daytime GS occurrence rate, Figure 5b, show more complex pattern, with larger variability. Overall, the minimal rates are consistently achieved in summer while the maxima are achieved around winter time, but not always close to December-January solstice time. Double-peaked curves are evident for winter of 2008-2009, 2009-2010, 2010-2011, 2011-2012 with occurrence rate maxima shifted towards equinoctial time, consistent with semi-annual anomaly behaviour (Themens et al., 2017, 2019).

Variations of daytime N_mF_2 also show multi-peaked features with maxima often occurring close to the equinoctial time. However, the local "dips" of N_mF_2 in winter solstices are not as strong as those for the occurrence rate. An increase in both occurrence rate and N_mF_2 at high solar activity is evident although enhancements of N_mF_2 seem to be much stronger. During low solar activity, peak-to-minimum ratios are larger for the occurrence rate, a factor of 2-3 versus a factor of 1.2-1.5 for N_mF_2. During high solar activity (2012-2015), peak-to-minimum ratios are larger for N_mF_2, a factor of 2-5 versus a factor of 1.2-1.5 for the GS occurrence rate. The Pearson correlation coefficient between variations of the occurrence rate and N_mF_2 for the entire considered period is 0.55 which is better than that for the nighttime.

From the SAS data presented in Figure 5 one can conclude that the major difference between the seasonal variations in GS occurrence rate during nighttime and daytime is that while the nighttime occurrence rate is maximized in summer, the daytime occurrence rate is enhanced rather in winter. This is consistent with the midlatitude Winter Anomaly (WA) phenomenon (e.g., Yasyukevich et al., 2018) that will be discussed later.

6. Seasonal variations of GS occurrence rate for some Northern Hemisphere SuperDARN radars

Now we compare seasonal variations of nighttime and daytime GS occurrence rates for a number of SuperDARN radars operated in the Northern Hemisphere at middle latitudes, i.e. where the WA is highly expected, Figure 6. We consider data for 2007-2018, the same period as for the SAS radar.

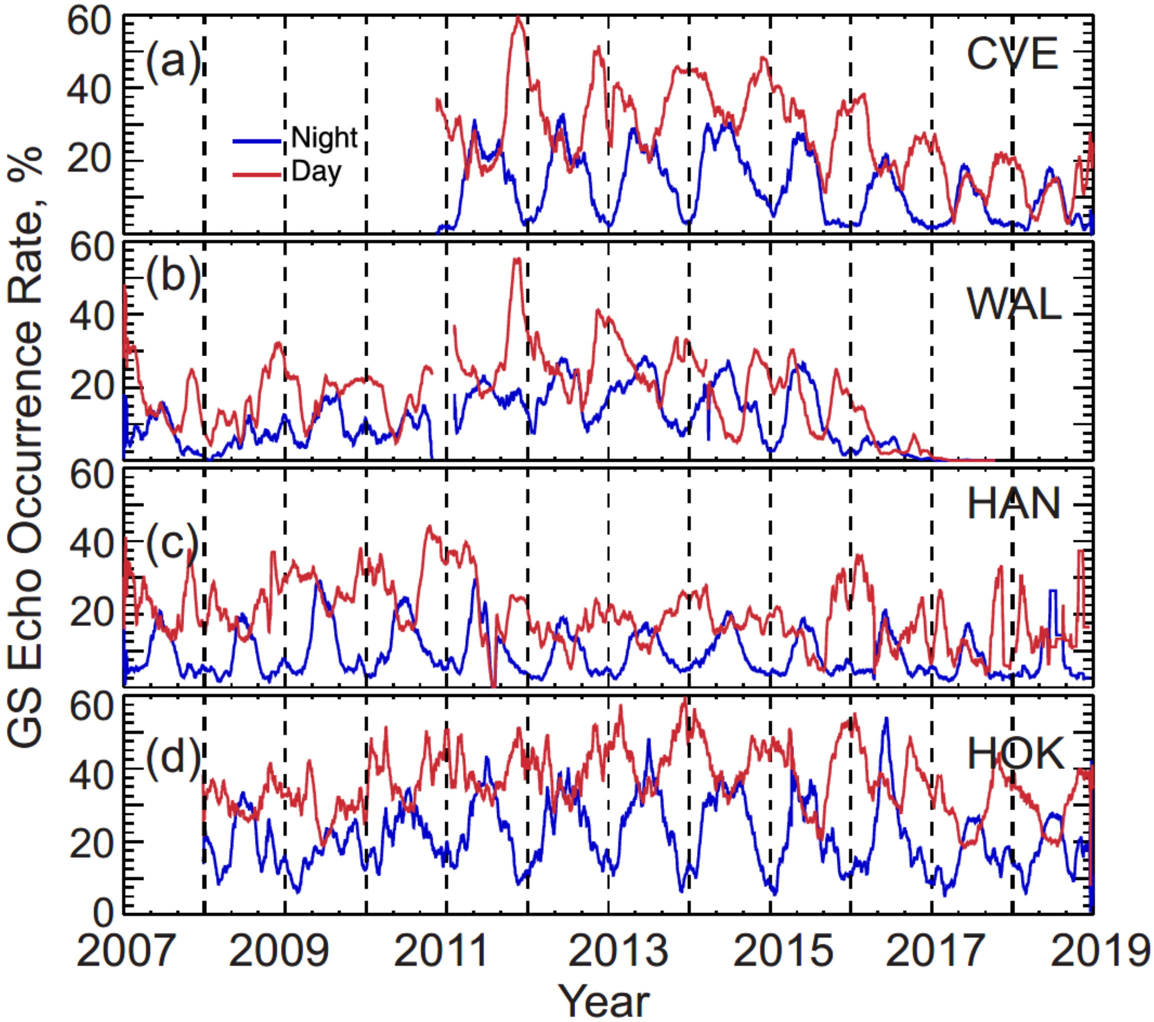

Figure 6: Line plots of the ground scatter (GS) occurrence rate for four SuperDARN radars in the Northern Hemisphere, Christmas Valley East (CVE), Wallops Island (WAL), Hankasalmi (HAN) and Hokkaido East (HOK). Observations in all beams and radar frequencies averaged over range gates 10-50 for (a) nighttime (0300 UT and 0900 UT, blue line) and (b) daytime (1500-2100 UT, red line) were considered. For some years, no data were available (gaps). The 15-min occurrence values were smoothed by applying a running 30-day boxcar filter.

Figure 6a for the Christmas Valley East (CVE) radar shows a clear "anticorrelation" of nighttime and daytime curves, with daytime maxima being achieved in winter and nighttime maxima being achieved in summer. Exceptional are 2017 and 2018 when additional daytime maxima are seen in summer.

Figure 6b for the Wallops Island (WAL) radar shows less clear patterns. Generally, the nighttime occurrence rate peaks are typically seen in summer while daytime occurrence rate peaks are seen in winter, but the enhancements are less smooth comparing to the CVE patterns of Figure 6a. This is particularly well seen for the nighttime data in 2007-2012.

Figure 6c for the Hankasalmi (HAN) radar in the European sector also shows daytime occurrence rate maxima in winter and nighttime occurrence rate maxima in summer. The daytime enhancements are weaker during 2012-2015, the period of high solar activity, and in 2017-2018. General decrease in maximum occurrence rates at HAN during high solar activity period of 2012-2015 is inconsistent with the data for other considered radars.

Figure 6d for the Hokkaido East (HOK) radar in the Japanese sector shows consistently summer maxima for nighttime occurrence rate. The HOK daytime data are more confusing; the enhancements/maxima, overall, are in winter but, for many years, there is significant variability of the GS occurrence rate with minor peaks at equinoctial time.

One can conclude that daytime GS occurrence rate is generally maximized predominantly in winter for the Northern Hemisphere midlatitude radars (CLE, HOK) and the auroral zone HAN radar.

7. Seasonal variations of GS occurrence rate for some Southern Hemisphere SuperDARN radars

Now we compare seasonal variations of nighttime and daytime GS occurrence rate for two Southern Hemisphere SuperDARN radars, TIGER (TIG) and Kerguelen (KIR), Figure 7, both in the Australian sector. The nighttime data for the TIG radar, Figure 7a, show clear local (in the Southern Hemisphere) summer maxima except for 2017-2018 when the rates dropped down dramatically. For the daytime, the seasonal variations of GS occurrence rate are not well defined although for some years, e.g. 2010-2015, the maxima occur in local winter. Data for the KER radar, Figure 7b, show tendencies similar to those for the TIG radar, namely more or less consistent summer maxima for nighttime and some winter enhancements for the daytime. We also processed data for the Falkland Islands (FIR) radar in the South American sector. Consistent with data reported earlier by Grocott et al. (2013), their Figure 5, daytime GS occurrence rates are highest in summer with some shift to equinoctial time.

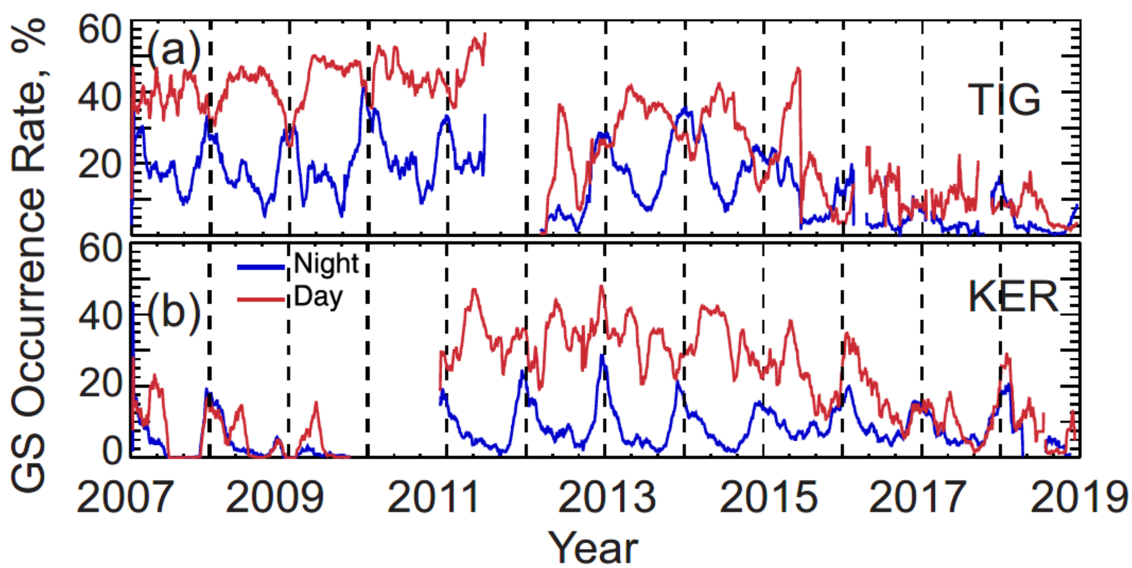

Figure 7: The same as in Figure 6 but for two Southern Hemisphere SuperDARN radars, Australian Tiger (TIG) and Kerguelen Island (KER).

One can conclude that daytime maxima in winter are less evident in the Australian sector and not seen in the South American sector.

8. Seasonal variations of GS occurrence rate for SuperDARN polar cap radars

Now we present GS occurrence rate data for the polar cap radars. We selected one radar in each hemisphere, the Inuvik (INV) radar in the Northern Hemisphere and the Dome C East (DCE) radar in the Southern Hemisphere, Figure 8. Both radars detect GS echoes predominantly in local summer, both on dayside and nightside. While the DCE daytime GS occurrence rate is higher at nighttime, the opposite holds for the INV radar.

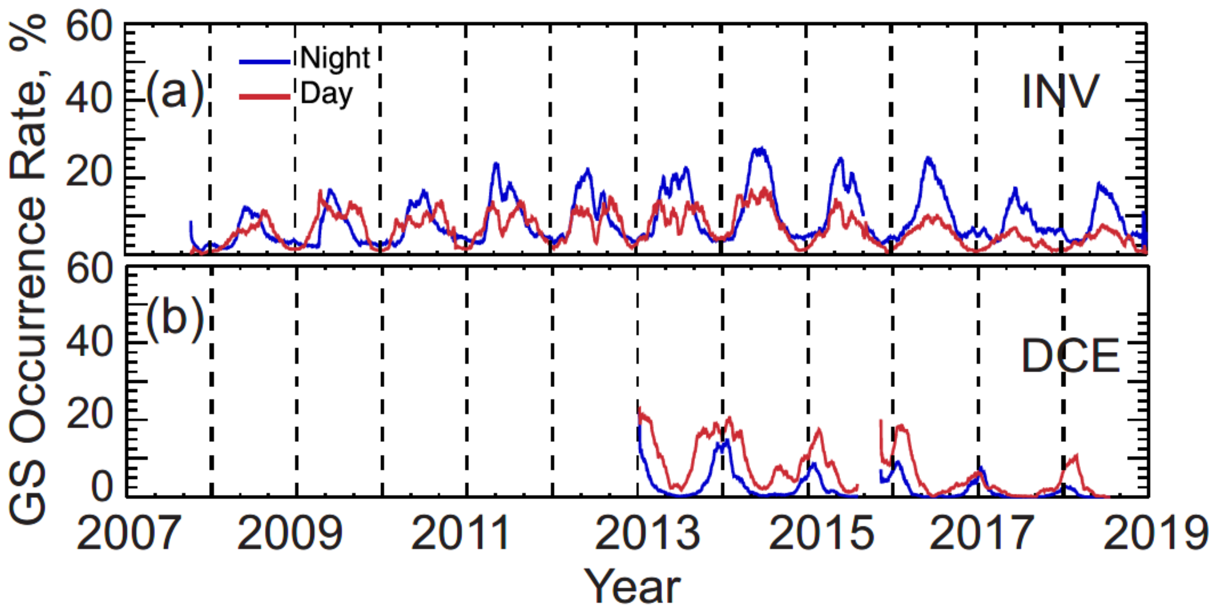

Figure 8: The same as in Figure 6 but for two polar cap SuperDARN radars, Inuvik (INV, Northern Hemisphere) and Dome C East (DCE, Southern Hemisphere).

9. Discussion

Reasons for variations in GS echo detection rate with the SuperDARN radars have not been discussed widely. Perhaps, to some extent, this is because of difficulty in assessing various factors affecting the echo detection rate.

One important aspect that gained attraction in recent publications (e.g., Burrell et al., 2018; Ponomarenko et al., 2009; Shand et al., 1998) is the fact that for successful GS echo detection, Earth's surface scatterers of the incoming radio waves must be present. These can be rocks, sharp edges of the landscape, or sea waves. The surface conditions vary with snow and ice coverage in winter. It has been known for years that GS echoes are not frequent for the Antarctic SuperDARN radars where the radio wave reflection from the ice shield is not effective (see, for example, DCE data in Koustov et al. (2019), their Figure 6 and HAN data in Milan et al. (1997), their Figure 7). The data presented in this study are in full agreement with previous findings regarding the important role of the ground scatterers. Our Figures 5-8 show directly that the polar cap DCE radar

(Antarctica) has the smallest GS occurrence rates. According to our analysis (data are not presented here, but some data are available in Koustov et al. (2019), their Figure 6) the McMurdo (Antarctica) radar has the lowest occurrence rates among all SuperDARN radars, two and more times smaller than those presented in Figure 8 and by Marcucci et al. (2021) for the DCN radar. This is not a surprise because the MCM radar transmits radio waves toward the mainland covered by ice all year around.

We demonstrated in this study that many features in variations of the GS occurrence rate cannot be explained by changes in the character of the surface reflectors. Data presented tells us that ionospheric propagation factors are also very important ones. For example, all the radars (but HAN) show a decrease in summer/winter echo occurrence rate peaks by a factor of 1.5-2 as the solar activity subsided from high in 2012-2014 to low in 2017-2018. These decreases are about the same in magnitude for the polar cap radars, SAS auroral zone radar and middle latitude radars. We expect that the surface reflectors within each radar field of view do not change dramatically over the years.

We also demonstrated in this study that seasonal variations in GS occurrence rate are not quite explainable by changes in the character of the surface reflectors. During nighttime and daytime, the reflectors are the same implying that seasonal variations of occurrence rate should be very similar for these time sectors of observations. This is not the case. For example, the SAS data for nighttime (Figure 5a) show systematic occurrence of smooth single-peaked enhancements centered in summer while the daytime data show mostly double-peaked maxima centered around winter with a minor dip usually coinciding with winter. Moreover, a GS occurrence rate single-peaked maximum at nighttime is a universal feature for observations of all the radars considered. The data for the daytime are less consistent. Double-peaked daytime maxima are seen for INV radar in the polar cap and HAN radar in the auroral zone. The midlatitude radars in the North American sector (Figure 6) show mostly single-peaked winter maxima during daytime and single-peaked summer maxima during nighttime. Thus, for these midlatitude radars the seasons for maximum GS echo occurrence rate are completely different, winter versus summer.

Our major message with the data presented is that ionospheric propagation factors affect occurrence rates of GS echoes in very significant way. As mentioned, these factors have always been kept in mind, but actual experimental data supporting this notion have been very limited so far (e.g., de Larquier et al., 2011; Nishitani et al., 2019). Perhaps the most direct evidence was presented by de Larquier et al. (2011) who reported enhanced GS echo detection by the Blackstone SuperDARN radar during summer evening hours, after the local sunset, that clearly correlated with enhancements of the ionospheric electron density as measured by the Millstone Hill incoherent scatter radar (their Figure 5).

Marcucci et al. (2021) presented data on GS occurrence rate for the polar cap DCE and DCN radars, located at the South Geomagnetic Pole and capable receiving echoes at magnetic latitudes of up to 65°. The study was focused on ionospheric echoes but presented data on the ground scatter allows one to make some conclusions. Data of their Figure 7 show that GS echoes are hardly detectable for the N_mF_2 (as given by the IRI ionospheric model within the DCE radar field of view) below $\sim 1.5 \cdot 10^{11}\,\mathrm{m}^{-3}$. They also found lowest GS occurrence rate rates for winter (their Figure 3) with strong solar cycle decrease in 2019 as compared to 2013-2014. This decrease is well recognizable in all time sectors. Marcucci et al. (2021) presented their data in MLT-MLAT coordinates that makes it not easy to compare daytime and nighttime differences. We perfomed analysis of DCN data in individual beams and sorted them according to the local time sectors, similarly to other SuperDARN radars considered in this study and found (data are not presented) that GS occurrence rates are maximized in local summer with daytime DCN maxima being shifted by a about a month toward the local fall equinox. Thus, in terms of seasonal variation, the DCN data are consistent with the DCE data.

Other SuperDARN publications gave direct or indirect evidence that the enhanced electron density is a major factor in GS echo detection. Milan et al. (1997) presented GS data for the HAN and Pikkvibaer (Iceland) radars for initial observations in 1995-1996, the period of low solar activity. The HAN nighttime data showed clear increase in echo detection in summer. The daytime data showed comparable GS occurrence rates for all seasons. We note that the presented data on critical frequency of the ionosonde f_0F_2 (their Figure 6) operated within the radar field of view do not show significant differences in values of daytime f_0F_2 between summer and winter while nighttime f_0F_2 are clearly larger in summer. The PYK radar showed clearly larger occurrence of daytime GS echoes in winter. Nighttime GS data seasonal differences were not obvious. Frissell et al. (2014) presented data on GS echo occurrence for the Blackstone radar for June 2010- May 2011. Their Figure 7 has saturated color, but one can recognize the less frequent occurrence of daytime echoes in summer months of May-August implying that daytime GS is more frequent in winter. The nighttime occurrence rates seem to be larger during equinoctial months of March-April and September-October. Grocott et al. (2013) presented data on GS echo detection with the Falkland Island (FIR) radar, their Figure 5. The radar clearly shows larger daytime echo detection rates in summer (December-January-February). At nighttime hours, a strong decrease of echo detection rates toward winter is obvious. Thus, for this radar, the GS dominates during summer months for both daytime and nighttime. We performed analysis of FIR data with our approach and confirmed the above results that we initially inferred from plots published by Crocott et al. (2013).

Another recent focus in SuperDARN research with respect to GS echoes has been on the identification of whether these echoes are detected from the front lobe or the back lobe of the radar antennae. Prominent are efforts with respect to the HAN radar (Barrell et al., 2015; 2018). It is important to keep in mind that this radar has been operated at radar frequencies < 10 MHz, i.e., at the low end of frequencies used by other radars for which significant portion of data are at 11 MHz and higher.

One idea pursued by Barrel et al. (2018) is that at high solar activity the electron density in the auroal zone/polar cap, monitored through the antenna front lobe, is large enough to support echo detection from this direction while at low solar activity it is not as high and many, especially at nighttime, echoes are actually coming often from the back lobe. Their Figure 4 shows that outside winter periods, GS echoes are mostly detected from front lobe during daytime and often from the back lobe during nighttime, irrespective of the solar cycle phase. The authors suggest that perhaps there is some enhancement of echo detection from the back lobe for high solar activity for equinoctial time, but it is hardly possible to quantify this judgement based on the data provided in their Figure 5. One solid conclusion by Burrell et al. (2018) is that daytime GS occurrence rate shows a clear decrease of the number of back lobe GS returns at high solar activity. Overall, however, the results by Burrell et al. (2018) indicate confusing solar cycle dependencies in terms of the ratio of returns from the front and back lobes.

The HAN data reported in our Figure 6c indicate that the solar cycle variation for all GS echoes (without separation them according to the direction of arrival) show annual variations but the relationship with the phase of the solar cycle is confusing. This is in contrast with the results for other SuperDARN radars for which a clear tendency for the decrease of GS echo occurrence at low solar activity is evident. Reasons for this difference requires further investigation.

In this study we, first of all, investigated the relationship in GS occurrence rate and N_mF_2 by directly comparing HF data and N_mF_2 data obtained for the region roughly corresponding to the ½ hop of the HF radio wave propagation paths, i.e. the region where the major radio wave bending toward the ground is expected to occur. Our Figure 3 shows that indeed the GS occurrence rate increases with the electron density in the ionosphere, as it has been expected. Our plot also shows that with the electron density increase, the rate of growth slows down or even saturates. This is expected because for the electron density close to the threshold of GS echo detection (sufficient radio wave bending), the radio wave bending is only effective at heights near the electron density profile peak h_mF_2. At larger electron densities, the bending occurs at heights below h_mF_2 and at closer to the radar ranges, for example, compare ray tracings in Figures 1a and 1b. Thus, we confirmed, for the first time experimentally, the critical role of having high-enough electron density for detection of GS echoes with the SuperDARN radars.

Expanding this idea, we compared seasonal variations of GS occurrence rate for the SAS radar and electron density N_mF_2 given by the E-CHAIM statistical model. Although the correlation between the two data sets was not great, the shape of the curves, speaking qualitatively, were the same with single-peaked near summer maxima at nighttime and often double-peaked maxima centered around winter solstice time at daytime. We hypothesize that the found discrepancies are not only because of the statistical nature of the E-CHAIM model but also because of some uncertainties in actual GS band location, and more detailed comparison might give a better agreement.

One consequence of the found occurrence rate- N_mF_2 correlation is that the enhancement in ground scatter occurrence rate could be an indicator of enhanced electron density in the ionosphere for specific conditions under consideration. de Larquier et al. (2011) have exposed this notion by looking at midlatitude evening anomaly and GS occurrence rate for the Backstone radar.

One important finding of our investigation is that the midlatitude SuperDARN radars in the North American sector show a clear GS occurrence rate daytime enhancement in winter, e.g. our Figure 6 and to some extent Figure 5. This effect was not seen in the nighttime sector. Importantly, the daytime winter enhancements were less clear in the European and Australian sectors and were not seen in the South American sector. These enhancements, or lack of enhancement, in GS occurrence rate are consistent with the well-known effect of electron density enhancements at midlatitudes known as winter anomaly, WA (e.g., Pavlov & Pavlova, 2005; Torr et al., 1980; Yasyukevich et al., 2018).

The WA is a ubiquitous midlatitude phenomenon in the North American sector. Recent paper by Yasyukevich et al. (2018) gives an extensive and detailed summary of WA studies. The essence of the phenomenon is in higher summer maximum electron densities at noon in winter as compared to that in summer, under comparable solar activity levels. The effect is strongest in North American sector, somewhat weaker in the Japanese sector, and even further weaker over Europe and in the Australian sector. WA is not evident in the South American sector. The data presented in this study thus show a great deal of similarity in terms of how the WA deteriorates as we go from the North American sector to Australian sector and to South American sector (Yasyukevich et al., 2018). In this sense, it is of great interest to investigate whether the daytime winter enhancements in GS occurrence rate occur in the Asian sector where Russian HF radar at Ekaterinburg (Berngardt et al., 2015) and new Chinese HF SuperDARN radar (Wang et al., 2022) have accumulated sufficient amount of data.

One worthy note is with respect to the WA effect for the HAN radar. Sodankyla ionosonde data presented by Ghezelbash (2013) show that the WA effect only present at high solar activity. It is then not a surprise that the HAN data on GS occurrence, Figure 6c, are confusing with respect to WA effect for 2017 and 2018.

10. Conclusions

In this study, we investigated two aspects of ground scatter detection with HF SuperDARN radars: 1) the correlation of the GS echo occurrence rate and the electron density in the ionosphere and 2) a general pattern in solar cycle and seasonal variations of GS occurrence rate at nighttime and daytime at various latitudes and longitudinal zones.

Obtained results can be summarized as follows:

- Occurrence rate of GS echo detection with the SuperDARN radar at Rankin Inlet increases with an increase of the peak electron density of the ionospheric F layer for N_mF_2 up to $\sim 4 \cdot 10^{11}\ \mathrm{m}^{-3}$. At larger N_mF_2, saturation in the trend is evident. These findings are consistent with the expectations from the ray tracings of radio wave paths in the ionosphere.

- GS occurrence rate for the midlatitude SuperDARN radars in the North American sector are maximized in winter at daytime but in summer at nighttime. The winter daytime maxima are less obvious in the European, Japanese, and Australian sectors and not seen in the South American sector. Winter maxima in occurrence of daytime echoes at midlatitudes are consistent with the winter anomaly phenomenon known for the maximum electron density in the F layer. Daytime maxima in GS occurrence rate for the auroral zone radars are often double-peaked with local peaks shifted toward local equinoxes.

- Daytime summer maxima or nighttime winter maxima in GS occurrence rate show solar cycle effect with reduced by a factor ~2 values at low solar activity periods, for most of the SuperDARN radars. The reduction also holds for the polar cap radars in both hemispheres.

- In the polar cap, the maxima of GS occurrence rate coincide with local summer seasons during both daytime and nighttime.

Acknowledgments

The SuperDARN data used in this work were collected with the support of the Canadian Space Agency's Geospace Observatory (GO Canada) continuation initiative, the Canada Foundation for Innovation, and the Province of Saskatchewan. The University of Calgary RISR-C radar is funded by the Canada Foundation for Innovation and is a partnership with the US National Science Foundation and SRI International who also fund RISR-C radar operation. The research was supported by an NSERC Discovery grant and Data Analysis Grant from Canadian Space Agency to A.V.K.

Data availability statement

Resolute Bay CADI ionosonde data can be downloaded from CHAIN website at http://chain.physics.unb.ca/chain/pages/cadi/. RISR-N/C data are available at the Madrigal database http://madrigal.phys.ucalgary.ca (both radars) or http://data.phys.ucalgary.ca (RISR-C). The data used in this work are also freely available through the NSF-supported Open Madrigal Initiative (http://cedar.openmadrigal.org/openmadrigal). SuperDARN data can be obtained online (https://superdarn.ca).

References

André, D., Sofko, G. J., Baker, K., & MacDougall, J. (1998). SuperDARN interferometry: Meteor echoes and electron densities from groundscatter. *Journal of Geophysical Research: Space Physics, 103*, 7003–7015. https://doi.org/10.1029/97JA02923

Berngardt O. I., Zolotukhina, N. A., & Oinats, A. V. (2015). Observations of field–aligned ionospheric irregularities during quiet and disturbed conditions with EKB radar: First results. *Earth, Planets and Space,* 67, 143. https://doi.org/10.1186/s40623-015-0302-3

Blanchard, G. T., Sundeen, S., & Baker, K. B. (2009). Probabilistic identification of high-frequency radar backscatter from the ground and ionosphere based on spectral characteristics. *Radio Science, 44,* RS5012. https://doi.org/10.1029/2009RS004141

Bland, E. C., McDonald, A. J., de Larquier, S., & Devlin J. C. (2014). Determination of ionospheric parameters in real time using SuperDARN HF radars. *Journal of Geophysical Research: Space Physics, 119*, 5830–5846. https://doi.org/10.1002/2014JA020076

Burrell, A. G., Milan, S. E., Perry, G. W., Yeoman, T. K., & Lester, M. (2015). Automatically determining the origin direction and propagation mode of high-frequency radar backscatter. *Radio Science, 50*, 1225–1245. https://doi.org/10.1002/2015RS005808

Burrell, A. G., Perry, G. W., Yeoman, T. K., Milan, S. E., & Stoneback, R. (2018). Solar influences on the return direction of high-frequency radar backscatter. *Radio Science, 53*, 577–597. https://doi.org/10.1002/2017RS006512

Cameron, T. G., Fiori, R. A. D., Themens, D. R., Warrington, E. M., Thayaparan, T., & Galeschuk, D. (2022). Evaluation of the effect of sporadic-E on high frequency radio wave propagation in the Arctic. Journal of Atmospheric and Solar-Terrestrial Physics, 228, 105826. https://doi.org/10.1016/j.jastp.2022.105826.

Chakraborty, S., Ruohoniemi, J. M., Baker, J. B. H., & Nishitani, N. (2018). Characterization of short-wave fadeout seen in daytime SuperDARN ground scatter observations. *Radio Science, 53*, 472–484. https://doi.org/10.1002/2017RS006488

Chisham, G., Lester, M., Milan, S. E., Freeman, M. P., Bristow, W. A., Grocott, A., et al. (2007). A decade of the super dual auroral radar network (SuperDARN): Scientific achievements, new techniques and future directions. Surveys of Geophysics, 28, 33–109. https://doi.org/10.1007/s10712-007-9017-8

Davies, K. Ionospheric Radio, volume 31 of Electromagnetics and Radar Series. Peregrinus, 1990. ISBN 9780863411861.

de Larquier, S., Ruohoniemi, J. M., Baker, J. B. H., Ravindran Varrier, N., & Lester, M. (2011). First observations of the midlatitude evening anomaly using Super Dual Auroral Radar Network (SuperDARN) radars. *Journal of Geophysical Research: Space Physics, 116*, A10321. https://doi.org/10.1029/2011JA016787

Fiori, R. A. D., Koustov, A. V., Chakraborty, S., Ruohoniemi, J. M., Danskin, D. W., Boteler, D. H., & Shepherd, S. G. (2018). Examining the Potential of the Super Dual Auroral Radar Network for Monitoring the Space Weather Impact of Solar X-Ray Flares. *Space Weather, 16*. https://doi.org/10.1029/2018SW001905

Frissell, N. A., Baker, J. B. H., Ruohoniemi, J. M., Gerrard, A. J., Miller, E. S., Marini, J. P., West, M. L., & Bristow W. A. (2014). Climatology of medium-scale traveling ionospheric disturbances observed by the midlatitude Blackstone SuperDARN radar. *Journal of Geophysical Research: Space Physics, 119,* 7679–7697. https://doi.org/10.1002/2014JA019870

Gillies, R. G., van Eyken, A., Spanswick, E., Nicolls, M. J., Kelly, J., Greffen, M., et al. (2016). First observations from the RISR-C incoherent scatter radar. *Radio Science, 51*, 1645–1659. https://doi.org/10.1002/2016RS006062

Ghezelbash, M., Fiori, R. A. D., & Koustov, A.V. (2014a). Variations in the occurrence of SuperDARN *F* region echoes. *Annales Geophysicae, 32*, 147-156. https://doi.org/10.5194/angeo-32-147-2014

Ghezelbash, M., Koustov, A. V., Themens, D. R., & Jayachandran, P. T. (2014b). Seasonal and diurnal variations of PolarDARN *F* region echo occurrence in the polar cap and their causes. *Journal of Geophysical Research: Space Physics, 119*, 10426–10439. https://doi.org/10.1002/2014JA020726

Ghezelbash, M. (2013). Occurrence and causes of *F*-region echoes for the Canadian PolarDARN/ SuperDARN radars. M. Sc. Thesis, University of Saskatchewan, 2013. http://hdl.handle.net/10388/ETD-2013-03-949.

Grocott, A., Hosokawa, K., Ishida, T., Lester, M., Milan, S. E., Freeman, M. P., Sato, N., & Yukimatu, A. S. (2013). Characteristics of medium-scale traveling ionospheric disturbances observed near the Antarctic Peninsula by HF radar. *Journal of Geophysical Research: Space Physics*, *118*, 5830–5841. https://doi.org/10.1002/jgra.50515

Jayachandran, P. T., Langley, R. B., MacDougall, J. W., Mushini, S. C., Pokhotelov, D., Hamza, A. M., et al. (2009). Canadian High Arctic Ionospheric Network (CHAIN). *Radio Science, 44*, RS0A03. https://doi.org/10.1029/2008RS004046

Karhunen T. J. T., Robinson, T. R., Arnold, N. F., & Lester, M. (2006). Determination of the parameters of travelling ionospheric disturbances in the high-latitude ionosphere using CUTLASS coherent scatter radars. *Journal of Atmospheric and Solar-Terrestrial Physics*, *68*, 558–567. https://doi.org/10.1016/j.jastp.2005.03.021

Koustov, A.V., Ullrich, S., Ponomarenko, P. V., Nishitani, N., Marcucci, M. F., & Bristow, W. A. (2019). Occurrence of *F* region echoes for the polar cap SuperDARN radars. *Earth, Planets, and Space, 71***,** 112. https://doi.org/10.1186/s40623-019-1092-9

Koustov, A. V., Ullrich, S., Ponomarekno, P. V., Gillies, R. G., & Nishitani, N. (2020a). Comparison of SuperDARN peak electron density estimates based on elevation angle measurements to ionosonde and incoherent scatter radar measurements. *Earth, Planets and Space, 72,* 43. https://doi.org/10.1186/s40623-020-01170-w

Koustov, A. V., Luciuk, M. R., Gillies, R. G., Ullrich, S., Larson, B., McWilliams, K. A., & Schmidt, M. T. (2020b). Velocity of SuperDARN echoes at intermediate radar ranges. *Radio Science, 55*, e2020RS007142. https://doi.org/10.1029/2020RS007142

Makarevich, R. A., Koustov, A. V., Igarashi, K., Ohtaka, K., Ogawa, T., Nishitani, N., Sato, N., Yamagishi, H., & Yukimatu, A. S. (2002). Comparison of flow angle variations of *E*-region echo characteristics at VHF and HF. *Advances in Polar Upper Atmosphere Research*, No 16, 59-83.

Marcucci, M. F., Coco, I., Massetti, S., Pignalberi, A., Forsythe, V., Pezzopane, M., Koustov, A., et al. (2021). Echo occurrence in the southern polar ionosphere for the SuperDARN Dome C East and Dome C North radars. *Polar Science, 28***,** 100684. https://doi.org/10.1016/j.polar.2021.100684

McDougall, J. W., Jayachandran, P. T., & Plane, J. M. C. (2000). Polar cap Sporadic-E: part 1, Observations. *Journal of Atmospheric and Solar-Terrestrial Physics, 62*, 1155-1167. https://doi.org/10.1016/S1364-6826(00)00093-6.

Milan, S. E., Jones, T. B., Robinson, T. R., Thomas, E. C., & Yeoman, T. K. (1997a). Interferometric evidence for the observation of ground backscatter originating behind the CUTLASS coherent HF radars. *Annales Geophysicae*, *15*, 29–39, https://doi.org/10.1007/s00585-997-0029-y.

Milan, S. E., Yeoman, T. K., Lester, M., Thomas, E. C., & Jones, T. B. (1997b). Initial backscatter occurrence statistics from the CUTLASS HF radars. *Annales Geophysicae, 15*, 703-718. https://doi.org/10.1007/s00585-997-0703-0

Milan, S. E., Grocott, A., de Larquier, S., Lester, M., Yeoman, T. K., Freeman, M. P., & Chisham, G. (2013). Traveling ionospheric disturbances in the Weddell Sea Anomaly associated with geomagnetic activity. *Journal of Geophysical Research: Space Physics*, *118*, 6608–6617. https://doi.org/10.1002/jgra.50566

Nishitani, N., Ruohoniemi, J. M., Lester, M., Baker, J. B. H., Koustov, A. V., Shepherd, S. G., et al. (2019). Review of the accomplishments of mid-latitude SuperDARN HF radars. *Progress in Earth and Planetary Science, 6(1),* 1–57. https://doi.org/10.1186/s40645-019-0270-5

Oinats, A. V., Nishitani, N., Ponomarenko, P., & Ratovsky, K. G. (2016). Diurnal and seasonal behavior of the Hokkaido East ground backscatter: simulation and observation. *Earth, Planets and Space, 68*, 18. https://doi.org/10.1186/s40623-015-0378-9

Pavlov, A. V., Pavlova, N. M. (2005). Causes of mid-latitude N_mF_2 winter anomaly at solar maximum. *Journal of Atmospheric and Terrestrial Physics, 67*, 862–877. https://doi.org/10.1016/j.jastp.2005.02.009

Ponomarenko, P. V., Menk, F. W., & Waters, C. L. (2003). Visualization of ULF waves in SuperDARN data. *Geophysical Research Letters*, *30*, 1926. https://doi.org/doi:10.1029/2003GL017757

Ponomarenko, P. V., Menk, F. W., Waters, C. L, & Sciffer, M. D. (2005). Pc3–4 ULF waves observed by the SuperDARN TIGER radar. *Annales Geophysicae*, *23*, 1271–1280. https://doi.org/10.5194/angeo-23-1271-2005

Ponomarenko, P. V., St-Maurice, J.-P., Hussey, G. C., & Koustov, A. V. (2010). HF ground scatter from the polar cap: Ionospheric propagation and ground surface effects. *Journal of Geophysical Research: Space Physics, 115*, A10310. https://doi.org/10.1029/2010JA015828

Ponomarenko, P. V., Iserhienrhien, B., & St.-Maurice, J.-P. (2016). Morphology and possible origins of near-range oblique HF backscatter at high and midlatitudes. *Radio Science*, *51*, 718–730. https://doi.org/10.1002/2016RS006088

Richards, P. G. (2001). Seasonal and solar cycle variations of the ionospheric peak electron density: Comparison of measurement and models. *Journal of Geophysical Research: Space Physics, 106*, 12803-12819. https://doi.org/10.1029/2000JA000365

Samson, J. C., Greenwald, R. A., Ruohoniemi, J. M., Frey, A., & Baker, K. B. (1990). Goose Bay radar observations of earth-reflected, atmospheric gravity-waves in the high-latitude ionosphere. *Journal of Geophysical Research: Space Physics*, *95*, 7693–7709. https://doi.org/10.1029/JA095iA06p07693

Shand, B. A., Milan, S. E., Yeoman, T. K., Chapman, P. J., Wright, D. M., Jones, T. B., & Pedersen, L. T. (1998). CUTLASS HF radar observations of the Odden ice tongue. *Annales Geophysicae*, *16*, 280–282.

Torr, D. G., Torr, M. R., & Richards, P. G. (1980). Causes of the *F* region winter anomaly. *Geophysical Research Letters*, *7*, 301–304. https://doi.org/10.1029/GL007i005p00301

Themens, D. R., Jayachandran, P. T., Galkin, I., & Hall, C. (2017). The empirical Canadian high arctic ionospheric model (E-CHAIM): N_mF_2 and h_mF_2. *Journal of Geophysical Research: Space Physics, 122*, 9015–9031. https://doi.org/10.1002/2017JA024398

Themens, D. R., Jayachandran, P. T., McCaffrey, A. M., Reid, B. & Varney, R. H. (2019). A bottomside parameterization for the Empirical Canadian High Artic Ionospheric Model (E-CHAIM), *Radio Sci.*, *54*, 397– 414. https://doi.org/10.1029/2018RS006748

Uspensky, M. V., Koustov, A. V., & Williams, P. J. S. (1993). The amplitude of auroral backscatter: III. Effect of tilted ionospheric layer. *Journal of Atmospheric and Terrestrial Physics*, *55*, 1383–1392. https://doi.org/10.1016/0021-9169(93)90106-9

Wang, W., Zhang, J. J., Wang, C., Nishitani, N., Yan, J. Y., Lan, A. L., et al. (2022). Statistical characteristics of mid-latitude ionospheric irregularities at geomagnetic quiet time: Observations from the Jiamusi and Hokkaido East SuperDARN HF radars. *Journal of Geophysical Research: Space Physics, 127,* e2021JA029502. https://doi.org/10.1029/2021JA029502

Watanabe, K., & Nishitani, N. (2013). Study of ionospheric disturbances during solar flare events using the SuperDARN Hokkaido radar. *Advances in Polar Science*, *24(*1), 12–18. https://doi.org/10.3724/SP.J.1085.2013.00012

Yasyukevich, Y., Yasyukevich, A., Ratovsky, K., Klimenko, M., Klimenko, V. V., & Chirik, N. (2018). Winter anomaly in N_mF_2 and TEC: when and where it can occur. *Journal of Space Weather & Space Climate, 8,* A45. https://doi.org/10.1051/swsc/2018036

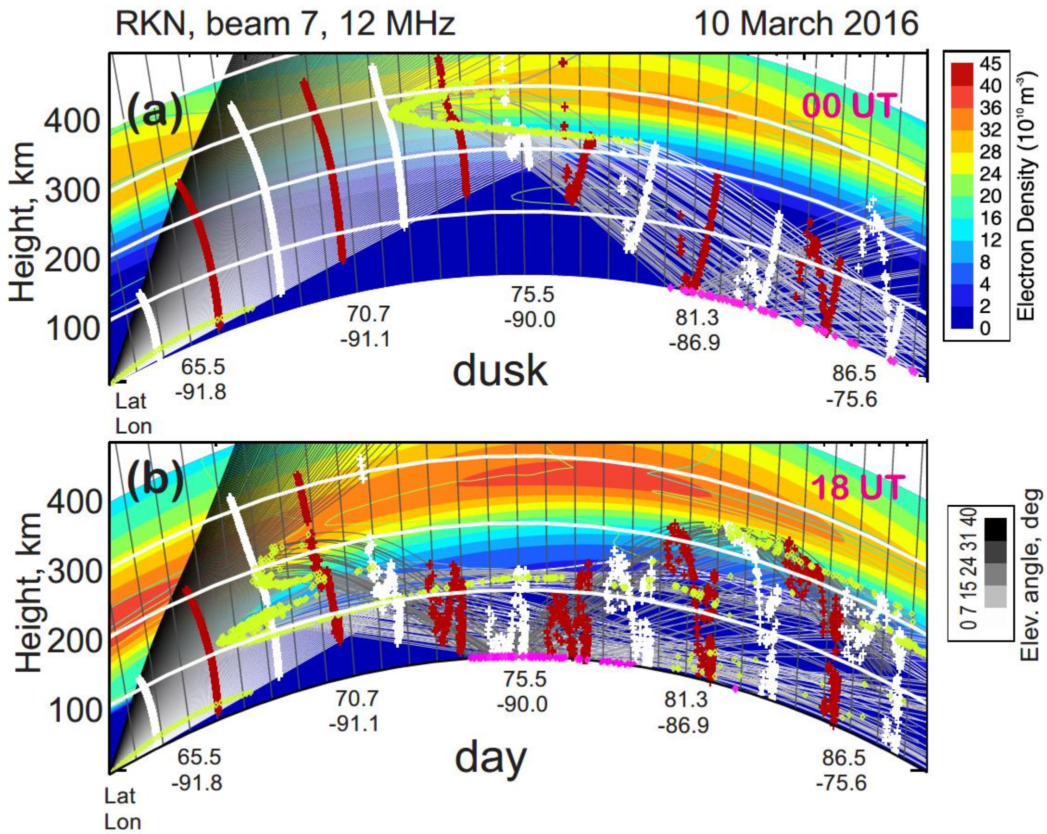

Figure 1: Ray tracing for 12 MHz radio waves transmitted by the Rankin Inlet (RKN) radar along its beam 7. The 2-D electron density distribution, represented by the color contours, is according to the E-CHAIM electron density model (Themens et al., 2017, 2019) with all values for (a) 00 UT and (b) 18 UT on 10 March 2016 increased by 1.25. White and red markers correspond to group range gates 0, 10, 20 … and 5, 15, 25…, respectively. Yellow markers at ionospheric heights mark those locations from where the ionospheric echoes can be detected while magenta markers on the ground are those locations from where the ground scatter echoes can be detected.

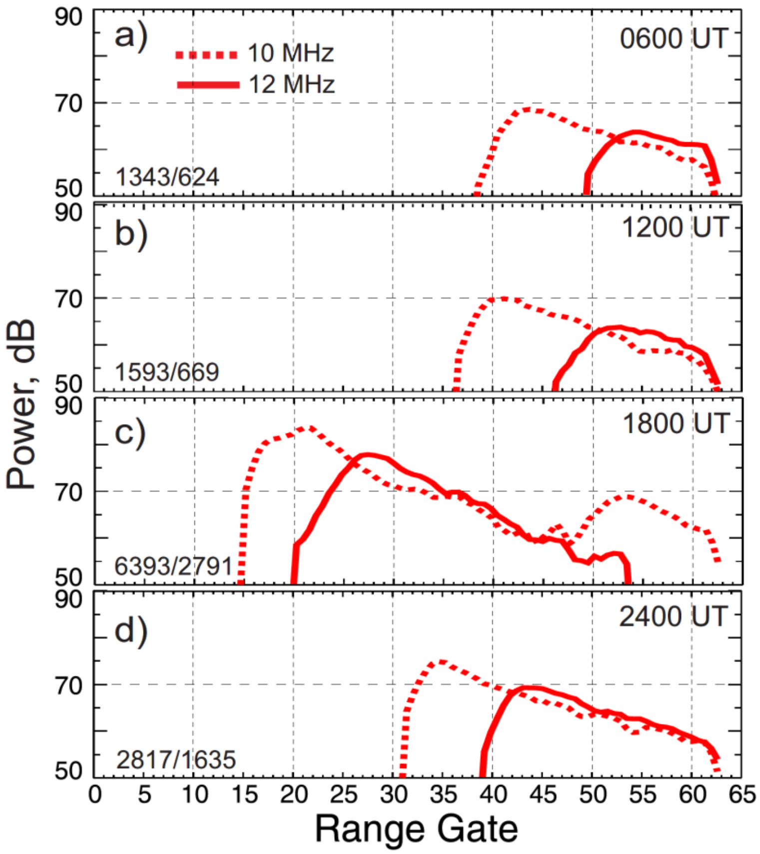

Figure 2: The expected power (in dB with respect to an arbitrary level) of ground-scattered echoes for various radar range gates of the SuperDARN Rankin Inlet (RKN) radar in beam 7 at operating frequencies of 10 and 12 MHz. Four panels correspond to observations the (a) midnight (06 UT), (b) dawn (12 UT), (c) daytime (18 UT) and (d) dusk (00 UT) sectors. A case of 10 March 2016 was considered (Figure 1 shows modeling for 00 UT and 18 UT). Details of the modelling approach are given in the text and in Koustov et al. (2020b). Numbers in the left-bottom corner of each panel indicate the total number of rays that formed the ground scatter range profiles at 10 and 12 MHz, respectively.

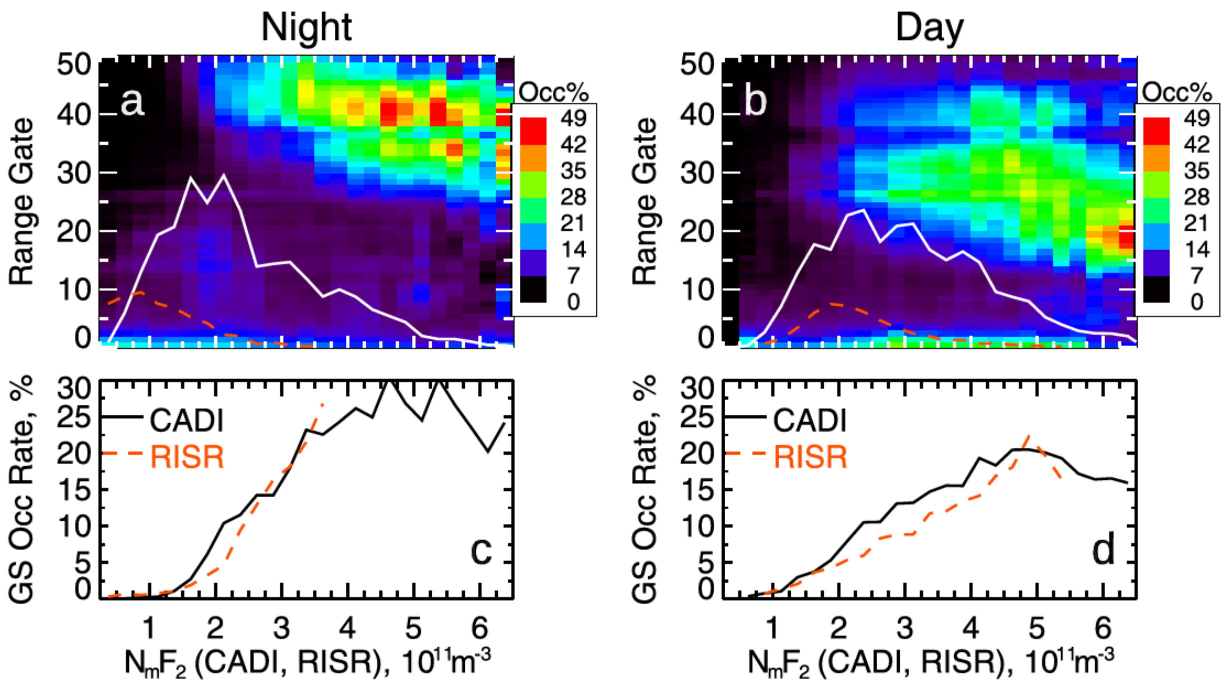

Figure 3: Ground scatter (GS) occurrence rate (over 15-min intervals) for the Rankin Inlet (RKN) SuperDARN radar observations in beams 4-6 at various range gates as a function of the *F* region peak electron density N_mF_2 measured concurrently by the Resolute Bay CADI ionosonde (a) for nighttime (03-09 UT) and (b) daytime (15-21 UT). Solid white lines indicate the number of available joint points (counts were divided by 40). (c) Line plot of the average GS occurrence rate over the band of ranges (gates 30-50 for nighttime and 20-40 for daytime), given as a solid line, versus N_mF_2 for joint observations with CADI at (c) nighttime and (d) daytime. N_mF_2 bins of 0.25×10^{11} m^{-3} were implemented. Dashed lines in all panels show the same dependence but for joint observations of the RKN and RISR radars.

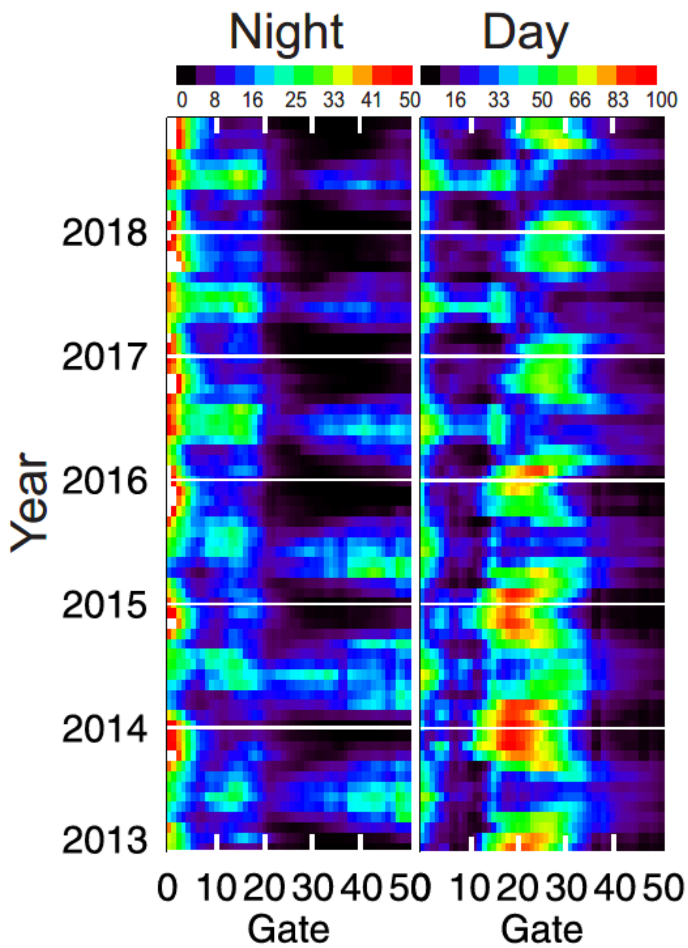

Figure 4: Occurrence rate of ground-scattered (GS) echo detection by the Saskatoon (SAS) SuperDARN radar at various ranges (range gates) in all beams irrespective of radar frequency for observations in 2013-2018. Left column are data for the nighttime (0300-0900 UT) while right column are data for daytime (1500-2100 UT). Notice that that the scale (color bars at the top) for the nighttime occurrence rate is half of that for the daytime occurrence rate.

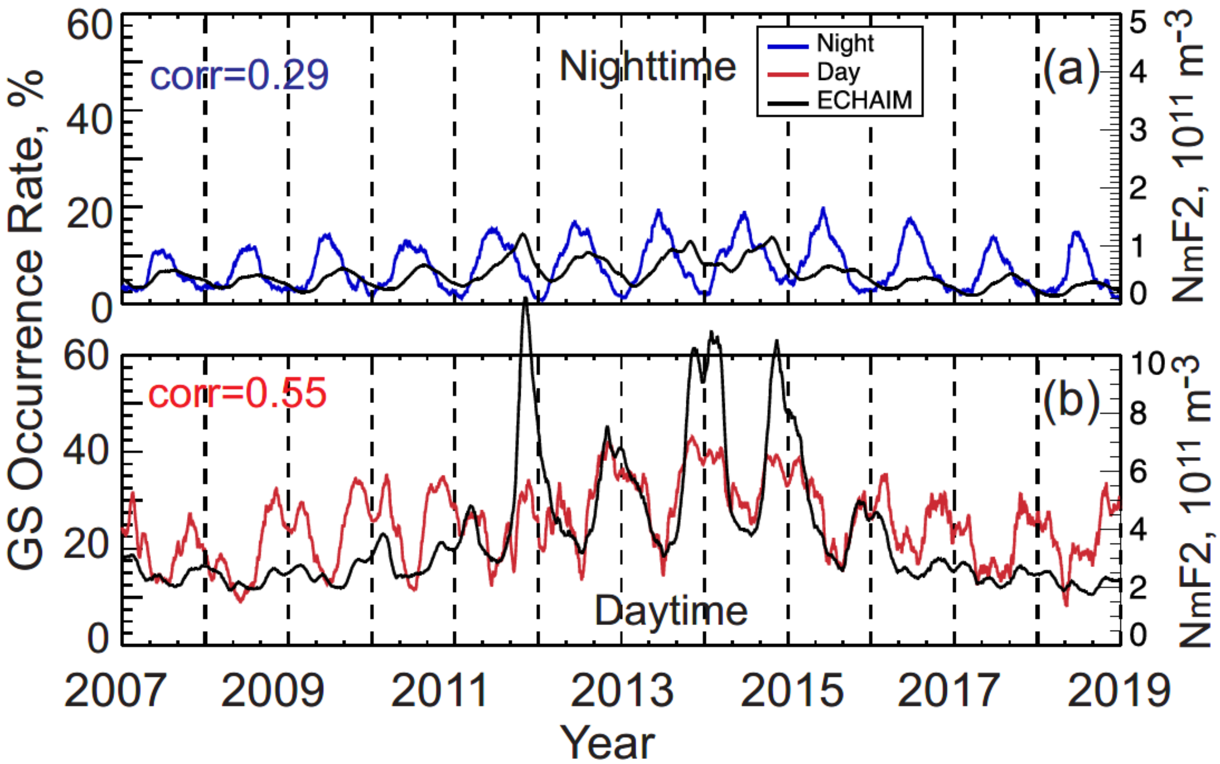

Figure 5: Line plots of the ground scatter (GS) occurrence rate for the Saskatoon SuperDARN radar in all beams averaged over range gates 10-50 for (a) nighttime (0300 and 0900 UT) and (b) daytime (1500-2100 UT) observations between 2007 and 2019. Transmissions on all radar frequencies were considered. The 15-min occurrence values were smoothed by applying a running +/- 15 day boxcar filter. Black line is the electron density N_mF_2 according to the E-CHAIM ionospheric model (Themens et al., 2017, 2019) computed for 15-min intervals and smoothed by applying a running +/- 15 day boxcar filter. In each panel, Pearson correlation coefficient (corr) between variations of the GS occurrence rate and N_mF_2 is presented.

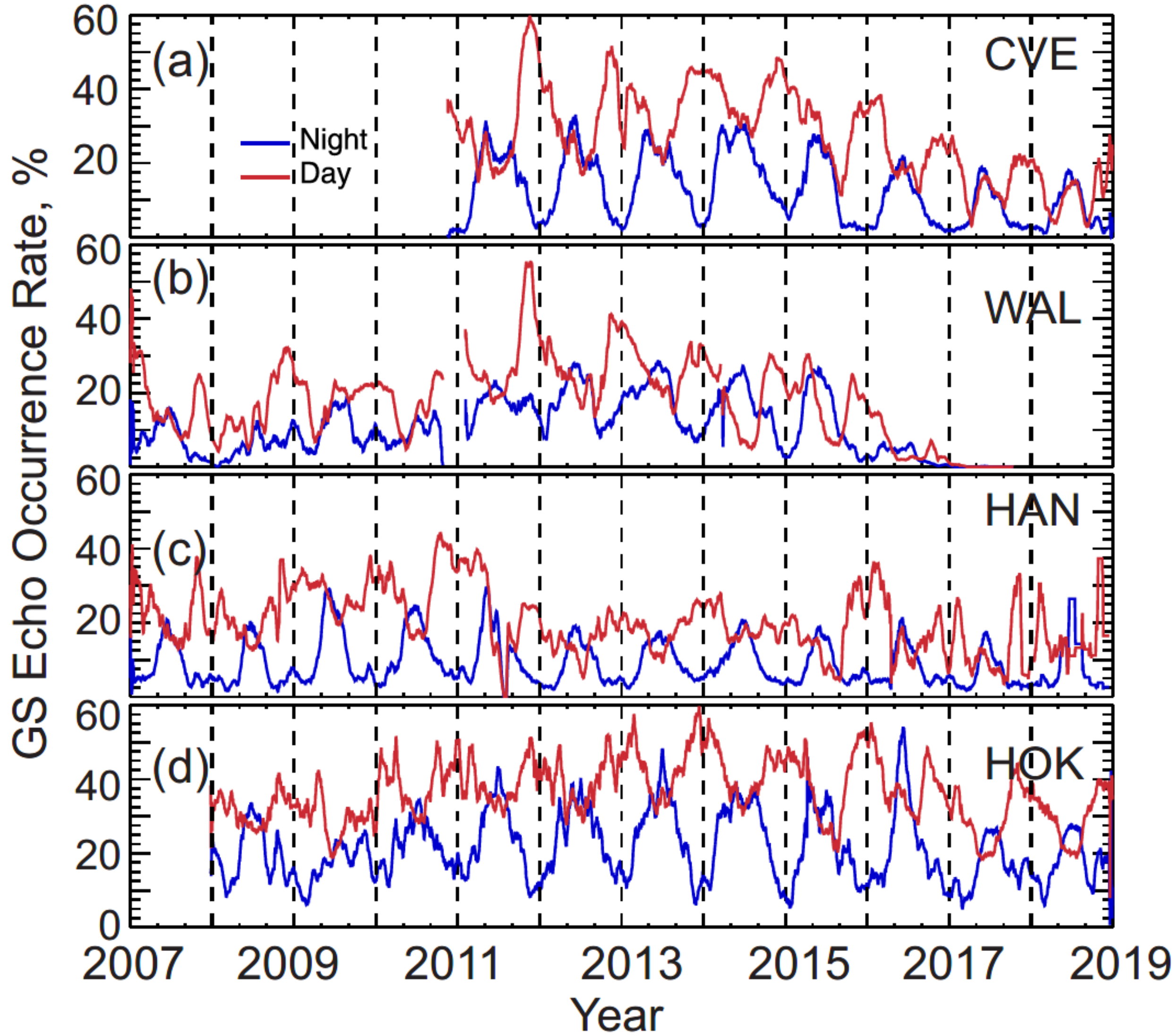

Figure 6: Line plots of the ground scatter (GS) occurrence rate for four SuperDARN radars in the Northern Hemisphere, Christmas Valley East (CVE), Wallops Island (WAL), Hankasalmi (HAN) and Hokkaido East (HOK). Observations in all beams and radar frequencies averaged over range gates 10-50 for (a) nighttime (0300 UT and 0900 UT, blue line) and (b) daytime (1500-2100 UT, red line) were considered. For some years, no data were available (gaps). The 15-min occurrence values were smoothed by applying a running 30-day boxcar filter.

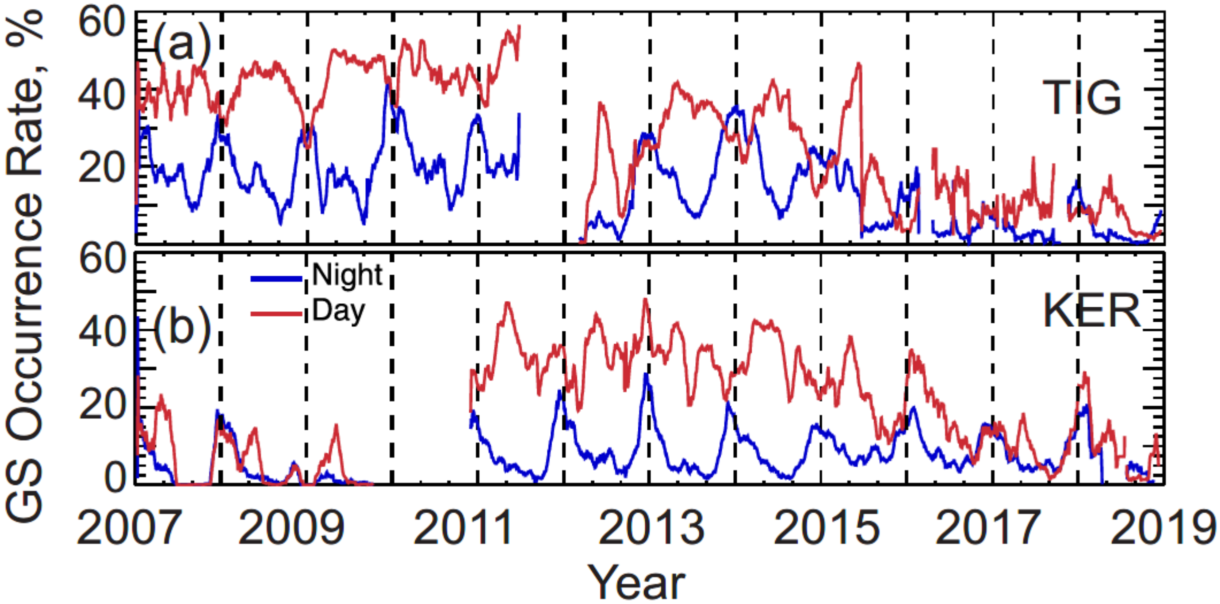

Figure 7: The same as in Figure 6 but for two Southern Hemisphere SuperDARN radars, Australian Tiger (TIG) and Kerguelen Island (KER).

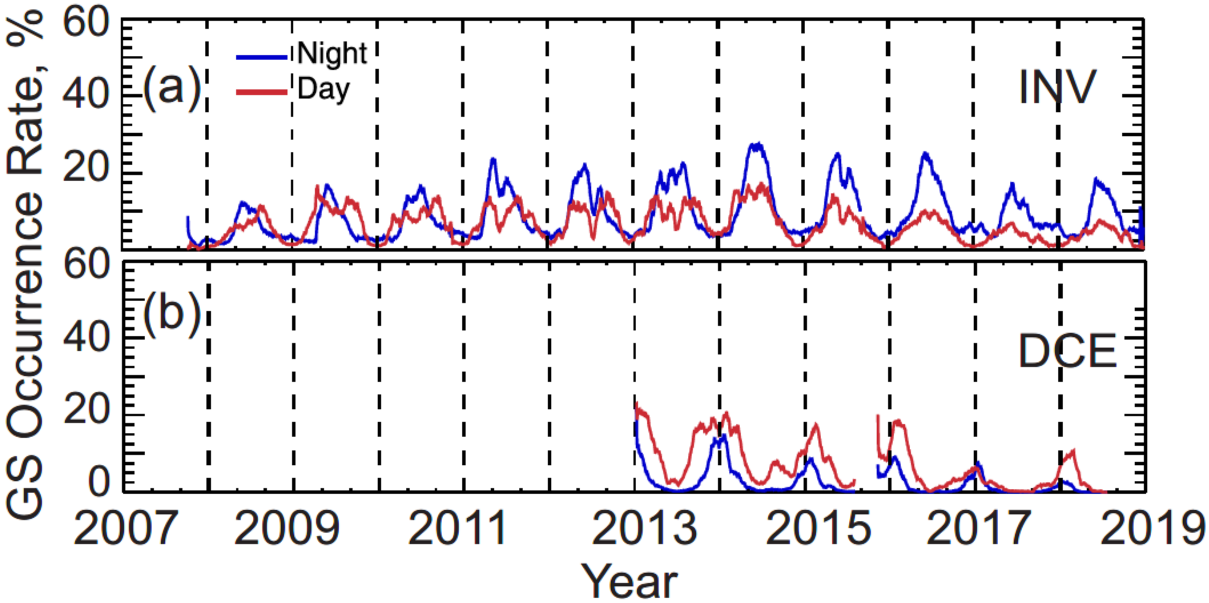

Figure 8: The same as in Figure 6 but for two polar cap SuperDARN radars, Inuvik (INV, Northern Hemisphere) and Dome C East (DCE, Southern Hemisphere).